Cavitating Propeller Flows Predicted by RANS Solver with Structured Grid and Small Reynolds Number Turbulence Model Approach

Tuomas Sipilä
VTT Technical Research Centre of Finland
Espoo, Finland

Timo Siikonen
Helsinki University of Technology (TKK)
Espoo, Finland

Ilkka Saisto
VTT Technical Research Centre
of Finland
Espoo, Finland

Jussi Martio
VTT Technical Research Centre
of Finland
Espoo, Finland

Heru Reksoprodjo
Helsinki University of
Technology (TKK)
Espoo, Finland

ABSTRACT

Within the EU research project VIRTUE, a propeller is investigated in uniform and non-uniform inflow conditions by means of a RANS equation solver, FINFLO. The analyses are made in wetted and cavitating conditions.

The propeller analyzed in this paper is the INSEAN E779A propeller. The paper contains calculations at three different grid resolutions in wetted conditions and at the two finest grid resolutions in cavitating conditions in uniform inflow. The medium-size grid is used for the propeller in non-uniform inflow simulations. The simulations are conducted on a model scale and the results are compared with the measurements and cavitation tests performed by INSEAN. The non-uniform inflow is generated by modeling the geometry of the artificial wake generator used in the cavitation tests in the calculation domain. The experimental results are published in several papers, for example in [1] and [2].

The predicted propeller open water thrust and torque are found to be within 5 % of the measured ones. The pressure peak at the leading edge of a blade is found to be sensitive to the grid resolution. The predicted cavitation behavior of the propeller blades is in reasonable accordance with the cavitation test observations. In uniform inflow the vaporized region is over-predicted. Contrastingly, the vaporized region is under-predicted in the non-uniform inflow calculations. Side entrant jets could be identified in the cavity region in the non-uniform inflow simulations. The predicted vaporized regions in several blade positions together with photographs of the cavitating propeller are shown for comparison. The cavitation behavior trends seemed to be similar in the simulations and observations in non-uniform inflow, except that the roll-up of detached sheet cavitation into a tip vortex could not be captured in the calculations.

The total wake is measured between the propeller plane and the wake generator. The predicted wake is found to be too strong, but the width of the wake is relatively close to the measurements. The propeller loading history is shown over one propeller revolution. It shows qualitatively reasonable trends. The loading histories of the wetted and cavitating propeller are almost the same due to the relative small cavitating region in the investigated conditions. The pressure distributions at several blade positions on the suction side of the propeller are shown in wetted and cavitating conditions for comparison.

INTRODUCTION

Cavitation produces a number of problems in propeller flows. The cavitating tip vortex collapse as well as the fluctuating type of sheet cavitation can cause noise in the interior of the ship and in the environment. The cavitation can also cause erosive behavior on propeller blades and on devices in the slipstream of the propeller, for example on rudders. In practice, a ship's propeller operates in an inhomogeneous wake field, where the velocity and direction of the flow in relation to the propeller blades vary during the rotation. For practical propeller analysis it is important to model both the cavitation phenomena and the unsteadiness of the inflow.

In the mid-1990s VTT Technical Research Centre of Finland started using FINFLO for propeller flow analyses [3]. In the present study FINFLO is used to simulate non-cavitating and cavitating propeller flows. The RANS equation solver – called FINFLO – is developed by Helsinki University of Technology (TKK) [4]. During recent projects, TKK has extended the FINFLO code to the simulation of multi-phase flows. At this stage the Merkle's mass transfer model for cavitating flows [5] is implemented for the phase transition.

The propeller analyzed in this paper is a modified Wageningen type propeller, the INSEAN E779A, which has an extensive experimental database [1], [2]. Because the test results of the propeller are very thoroughly documented, it was

also selected as a validation case in the EU project VIRTUE. Previous computational studies in VIRTUE workshops are reported in [6] and [7]. The cavitation tests are made in the Italian Navy's cavitation tunnel (CEIMM).

In this paper VTT Technical Research Centre of Finland has validated the multi-phase FINFLO code for homogenous inflow in wetted and cavitating conditions. In the simulations of non-uniform conditions the wake field was generated by modeling the test arrangement of five flow-oriented parallel flat plates.

In the results predicted global performance factors such as propeller thrust and torque are compared with measurements. The pressure distributions and coefficients of wetted and cavitating condition are compared. Finally, the predicted cavitation region is set against the observed ones in the cavitation tests.

NUMERICAL METHOD

FINFLO code

Flow simulation in FINFLO is based on the solution of the RANS equations by the pseudo-compressibility method. FINFLO solves the RANS equations by a finite volume method. The solution is based on the approximately factorized time-integration with local time stepping. The code uses either Roe's flux difference splitting or van Leer's flux-vector splitting for compressible flows, and an upwind-based scheme for incompressible flows that includes a cavitation model. A third order biased upwind scheme was utilized for the discretization of the convection terms, while a second order central-difference scheme was used for the discretization of the diffusion terms. In its implementation, FINFLO solves for the pressure, instead of density, which is assumed to be a function of pressure and enthalpy (or temperature). Finally, turbulence modeling is employed using the low Reynolds number k-ε model of Chien [8].

For the two-phase flow simulations, it is assumed that the flow is essentially isothermal, decoupling the energy equation from the system. Furthermore, a homogeneous assumption that both phases share the same velocity field is applied, which in turn also simplifies the turbulence modeling. The system of equations can then be expressed as follows:

$$\frac{\partial \rho_m}{\partial t} + \nabla \cdot \rho_m \vec{V} = 0 \qquad (1)$$

$$\frac{\partial \rho_m \vec{V}}{\partial t} + \nabla \cdot \rho_m \vec{V}\vec{V} + \nabla p = \nabla \cdot \overset{t}{\tau} \qquad (2)$$

$$\frac{\partial \alpha_v \rho_v}{\partial t} + \nabla \cdot \alpha_v \rho_v \vec{V} = -\Gamma, \qquad (3)$$

where ρ_m and ρ_v are the mixture (liquid and vapor) and vapor densities, respectively, $\vec{V}$ is the (shared) velocity, p is the pressure, and $\overset{t}{\tau}$ is the viscous stress tensor. In addition, α_v and Γ are the volume fraction of the vapor phase and the mass transfer terms, respectively. Conversely, the liquid phase volume fraction can be expressed as $1 - \alpha_v$.

Cavitation model

The cavitation modeling in FINFLO is based on the Merkle's mass transfer model [5]:

$$\Gamma = \frac{C_{dest}\rho_l \alpha_l \min[0, p - p_{sat}]}{\frac{1}{2}\rho_\infty V_\infty^2 \left(L_{ref}/V_\infty\right)} +$$
$$+ \frac{C_{prod}\rho_g \alpha_g \max[0, p - p_{sat}]}{\frac{1}{2}\rho_\infty V_\infty^2 \left(L_{ref}/V_\infty\right)}, \qquad (4)$$

where ρ_l and ρ_g are the density of the liquid phase and gas phase respectively, L_{ref} is the reference length, V_∞ is the free stream velocity and C_{dest} and and C_{prod} are the parameters for the cavitation model. Furthermore, the saturation pressure p_{sat} is obtained from a curve fit. The saturation pressure is determined according the Antoine's equation as follows:

$$\log p_{sat} = A - \frac{B}{T_{sat} + C}, \qquad (5)$$

where A,B,C are the parameters to be computed from the experimental values [9].

The variation of pressure is calculated by summing the density-weighted mass residuals of the gas phase and the liquid phase together. In order to avoid the problems related to the density difference between these two phases, the mass transfer term is pseudo linearized. The velocity change is determined by combining the mass residual and the explicit momentum residual.

The void fractions are updated at the implicit stage. This is accomplished by transforming the explicit residual to the primitive form and by applying some limitations to the mass transfer rate in order to avoid instabilities during the iteration process. Once the implicit residuals $\delta p, \delta \vec{V}, \text{and} \, \delta x_g$ are known, the solution can be obtained using the standard FINFLO preconditioning method. Also, the energy residuals are determined by the solver, but they are set explicitly as zeros.

Grid and boundary conditions

In the uniform inflow calculations the square tunnel cross section is simplified to be circular. The circular tunnel cross section allows a quasi-steady approach to be used because of the symmetry of the problem.

The tunnel radius is R_{tun} = 0.3344 m, which gives the same cross-sectional area as the actual tunnel. The domain length is 2.6 m, which refers to the actual length of the tunnel. The propeller plane is located in the middle of the domain. Figure 1 shows the calculation domain, the propeller and the axis location inside the tunnel. The propeller is run from upstream. Only one fourth of the whole tunnel is modeled due to the symmetry of the problem.

The blades and hub are modeled as no-slip rotating surfaces. The axis is modeled as a no-slip stationary surface. The tunnel roof is modeled as a slip wall. The velocity boundary condition is applied at the inlet, and the pressure boundary condition is used at the outlet. At the sides of the domain the cyclic boundary condition is applied.
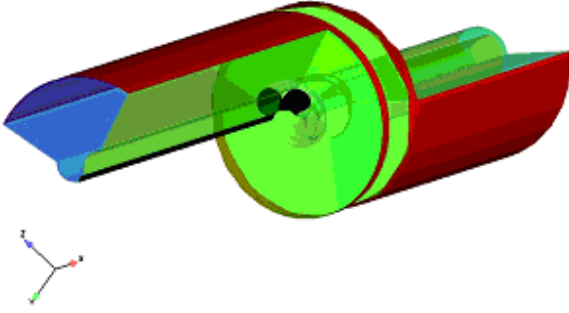
Figure 1: Calculation domain in uniform inflow calculations. ¼ of the whole domain is modeled because of the symmetry of the problem. The inlet is on the left-hand side and the outlet on the right-hand side. The propeller and the upstream located shaft are drawn in black color.

The uniform inflow calculations are performed at three grid levels in wetted conditions, and at the two finest grid levels in cavitating conditions. At coarser grid levels every second grid point is taken into account in every direction compared to the finer level grid. The solution for the coarser grid level is used as the initial guess in the finer grid level calculations.

The finest grid level consists of a total of 1.7 million cells in 12 blocks. The second and third level grids consist of 214 000 and 27 000 cells, respectively. On the blade surface the finest grid level consists of 144 cells in the chordwise direction and 104 cells in the spanwise direction. Especially, the grid resolution around the blade leading edge is high. At the finest grid level there are about 20 cells around the blade's leading edge radius. Because of the O-O topology, the same resolution is applied also around the blade tip and trailing edge. The grid is refined normal to the viscous surfaces so that the non-dimensional wall distance y^+ is close to unity at the finest grid level.

Table 1 gives a summary of the grid size details for the three grid levels. Figure 2 shows the grid on the blade surface and around the leading edge at a constant grid index at radius $r/R = 0.7$ for the three grid levels.

Table 1: Summary of grid size details for the three grid levels in uniform inflow calculations.

	Fine grid	Medium grid	Coarse grid
Total number of cells	1 710 592	213 824	26 728
Surface cells in chordwise direction (on one side)	144	72	36
Surface cells in spanwise direction (on one side)	104	52	26
Surface cells around leading edge radius	20	10	5
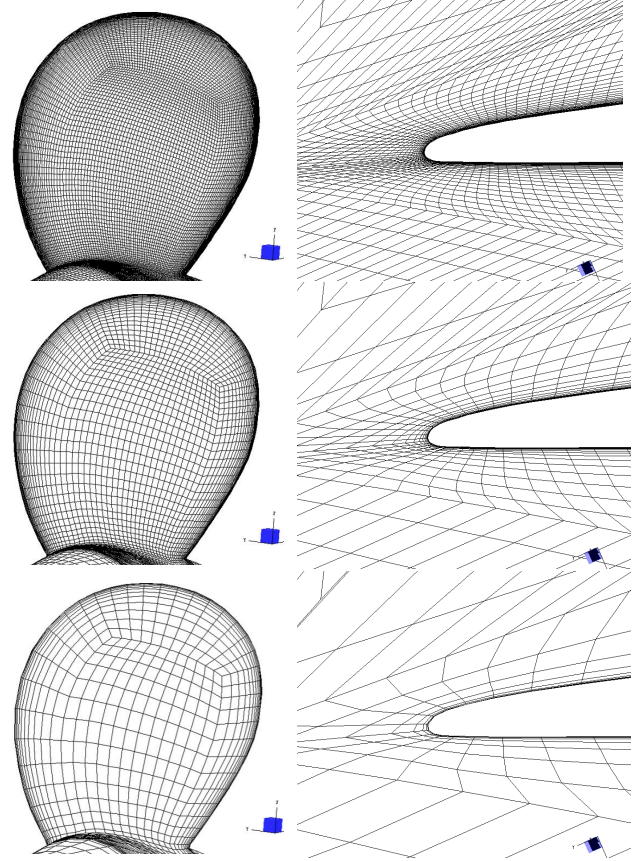
Figure 2: Grid resolution at three grid levels. In the left column: surface grid on blade. In the right column: grid near leading edge at constant grid index at radius $r/R = 0.7$. From top to bottom: first level fine grid, second level medium grid, and third level coarse grid.

The computational domain of the propeller in the wake field simulations consists of the actual tunnel geometry with a square tunnel cross section and roundings in the tunnel corners. The tunnel height is 0.6 m and the length is 2.6 m. The tunnel walls are modeled as slip surfaces to reduce the number of cells in the grid. The blades and the hub are no-slip rotating surfaces and the shaft is a no-slip stationary surface.

The wake to the propeller is created by modeling the actual geometry of the wake generator used in the cavitation tests. The wake generator consists of five flat plates parallel to the axial direction and 60 horizontal bars keeping the plates together. All parts of the wake generator are modeled as no-slip stationary surfaces. The wake generator is located so that its trailing edge is at $x/R = -0.89$ upstream from the propeller plane.

Since the propeller is working in a wake field the problem is not symmetrical and the whole domain must be modeled. The solution is unsteady and it must be solved with the time-accurate method. Part of the domain is rotating at the rotational speed of the propeller. The upstream location of the rotating domain is in the middle of the trailing edge of the wake generator and the propeller plane. The rotating domain extends to the outlet of the whole domain in the axial direction. In the radial direction the rotating domain extends to

about half way between the propeller tip and the tunnel roof. The rest of the domain is stationary. The sliding mesh boundary condition is applied at the interface of the rotating and stationary domains. The time-step in the calculations corresponds to 0.5° of propeller revolution. Figure 3 shows the calculation domain used in the simulation.

The grid near the propeller blades is the same as in the propeller in uniform inflow simulations. The simulations are performed only on the second level medium grid, which consists of about 1.3 million cells in 132 blocks. The first level fine grid would consist of about 10.5 million cells. Figure 4 shows the surface grid of the propeller, axis, and wake generator for the second level medium grid. Some of the horizontal bars keeping the plates together are also seen in Figure 4.
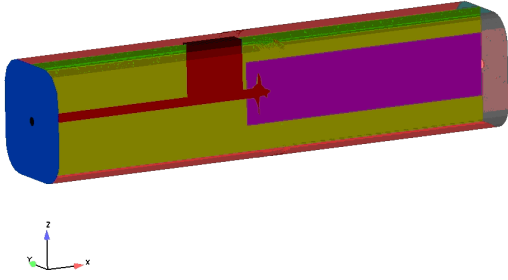
Figure 3: The calculation domain for the propeller in wake simulations. The inlet is on the left and outlet on the right. The wake generator, propeller and shaft are drawn in black color. The stationary part of the domain is colored green and the rotating part purple inside the domain.
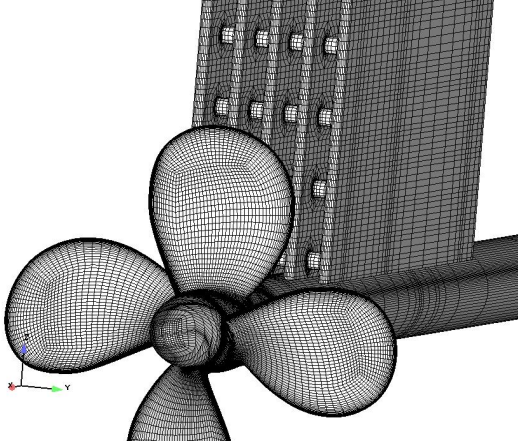
Figure 4: The surface grid of the propeller and the wake generator for the second level medium grid. The inflow to the propeller comes through the wake generator.

RESULTS

Propeller in uniform inflow

The propeller in uniform inflow is calculated in wetted and in cavitating conditions. The cavitation number in the investigated case is $\sigma_n = 1.763$, where σ_n is defined as

$$\sigma_n = \frac{p_\infty - p_v}{\frac{1}{2}\rho_w (nD)^2}, \tag{6}$$

where p_∞ is the pressure at infinity, ρ_w the water density, n the propeller rotational rate (36 rps), and D the propeller diameter (0.22727 m).

Propeller performance is given in Table 2 at advance number J = 0.71 in wetted and cavitating conditions. The advance number is specified as

$$J = \frac{V_{in}}{nD}, \tag{7}$$

where V_{in} is the inflow velocity. Thrust T and torque Q are non-dimensionalized, as is usual in the propeller field:

$$K_T = \frac{T}{\rho_w n^2 D^4} \tag{8}$$

and

$$K_Q = \frac{Q}{\rho_w n^2 D^5}. \tag{9}$$

The open water efficiency η_O is calculated as

$$\eta_O = \frac{J}{2\pi} \frac{K_T}{K_Q}. \tag{10}$$

The predictions are given for three grid levels in wetted conditions and for the two finest grid levels in cavitating conditions. The measurements of undisturbed inflow in wetted conditions have been conducted in a towing tank in open water conditions, and in a cavitation tunnel without the wake generator. In the cavitation tunnel the propeller is run from upstream. Because of the particular calibration technique used in the tunnel measurements the difference between measured thrust and torque in open water (towing tank) and tunnel conditions is about 8 % [7]. The calculated propeller thrust and torque are compared with the open water measurements below.

It is seen that the calculated thrust and torque in wetted conditions are under-predicted by 4.6 and 4.9 per cent, respectively, at the finest grid level. The predicted efficiency at the finest grid level is very close to the measurements. It is seen that the predicted torque is more sensitive than the thrust to the grid resolution.

Table 2: Measured and calculated global propeller performance for three grid levels in wetted conditions and for two grid levels in cavitating conditions at J = 0.71. The measured values are also shown.

	K_T	$10\,K_Q$	η_O
Wetted condition			
Fine grid	0.227	0.408	0.629
Medium grid	0.226	0.414	0.618
Coarse grid	0.230	0.430	0.604
Measurements			
tunnel	*0.256*	*0.464*	*0.623*
open water	*0.238*	*0.429*	*0.627*
Cavitating condition $\sigma_n = 1.763$			
Fine grid	0.261	0.469	0.629
Medium grid	0.238	0.435	0.618
Measurements			
tunnel	*0.255*	*0.460*	*0.626*

Furthermore, it is seen that cavitation has very little influence on the propeller thrust and torque in the measurements. That is not the case in the simulations. Compared to the wetted condition, the predicted thrust and torque increase in cavitating conditions by 15 % at the finest grid level.
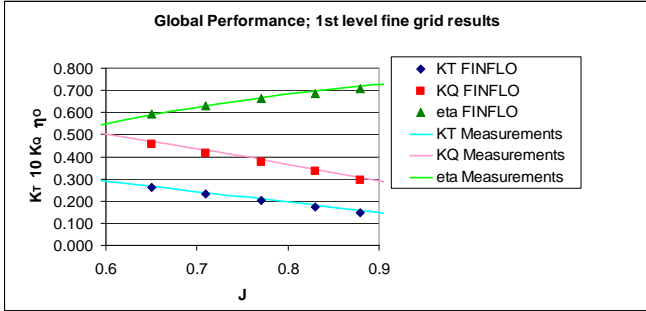

Figure 5: Measured and calculated global propeller performance in wetted conditions. The calculated results are for the first level fine grid.

Figure 5 shows the predicted and measured propeller thrust, torque, and efficiency over a range of advance numbers in the wetted conditions. The predicted thrust and torque are close to the measured ones over the whole range of advance numbers.

Figure 6 and Figure 7 reveal the reason for the increment in thrust and torque in the cavitation simulations. Figure 6 shows the pressure distribution on the blade suction and pressure sides in wetted and cavitating conditions at J = 0.71. The pressure difference is non-dimensionalized as follows:

$$C_p = \frac{p - p_\infty}{\frac{1}{2}\rho_w (nD)^2} . \tag{11}$$

Cavitation spreads the low pressure area excessively over the larger region of the blade compared to the wetted condition simulations, which increases the pressure force on the blade.
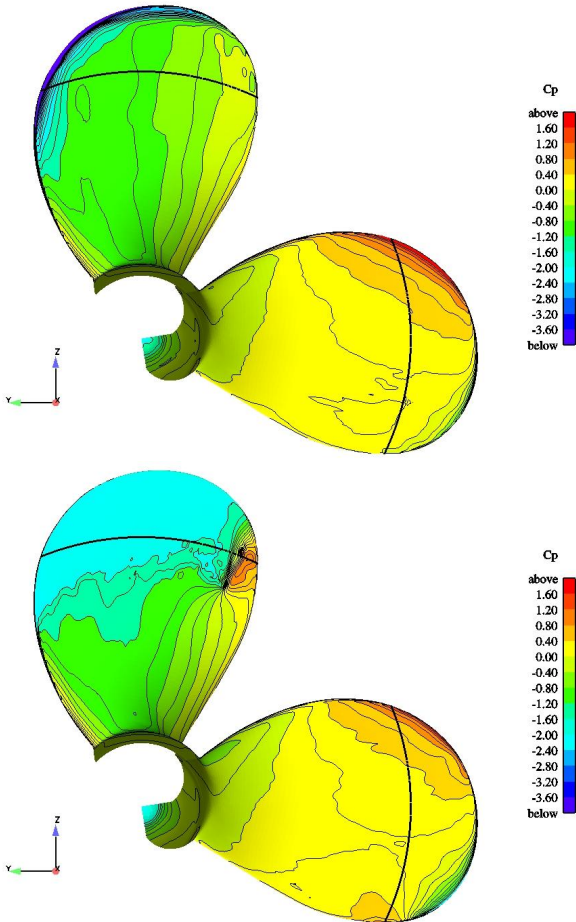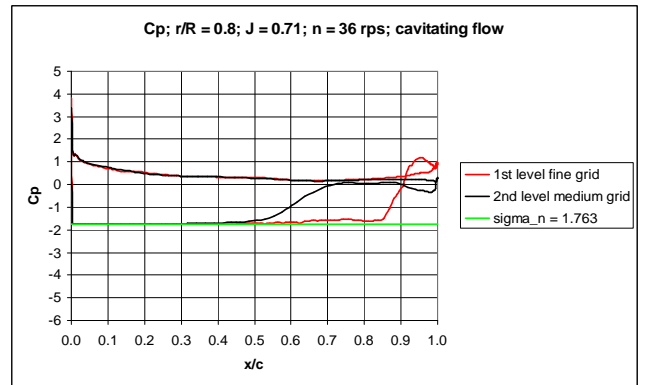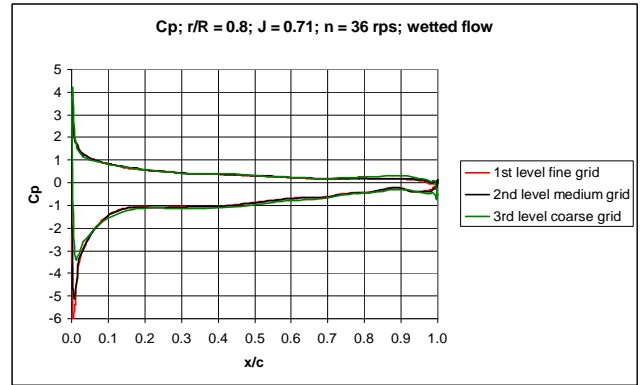

Figure 6: Pressure distribution on blade suction and pressure sides for the wetted condition (top) and for the cavitating condition (bottom) at J = 0.71. The figures are from the first level fine grid results. The thick black circular lines refer to radius r/R = 0.8

Figure 7: Pressure coefficient at radius r/R = 0.8 for the wetted condition (top) and for the cavitating condition (bottom) at J = 0.71. The result for the wetted condition is given for three grid levels and for cavitating condition for two grid levels. The cavitation number is also drawn to the bottom figure for reference

Figure 7 gives the 2D pressure distributions for the three grid levels in wetted conditions and for the two finest grid levels in cavitating conditions. For the wetted condition it is seen that the low-pressure peak is strongly dependent on the grid resolution around the leading edge. The low-pressure peak in the coarse grid (C_p = -3.4) is about half of that at the finest grid level (C_p = -6.1). The difference between low-pressure peaks in the second level medium grid (Cp = -5.1) and the first level fine grid is rather large, which raises a doubt as to whether a full grid convergence is reach for the pressure peak at the finest grid level. It is important to predict the pressure peak correctly from the cavitation inception point of view. Anyway, the grid convergence for the leading edge

pressure peak is thought to be reasonable at the finest grid level and no more refinement studies are made in this work. In the regions outside the leading edge the pressure distributions are very close to each other at all grid levels. Similar conclusions concerning the effect of grid refinement on the pressure distributions are made, for example, in [10].

Figure 7 also shows the 2D pressure distribution at radius r/R = 0.8 in cavitating conditions. It is seen that the low-pressure peak is cut at the saturation pressure $C_p = -\sigma_n = -1.763$. At the finest grid level, cavitation extends closer to the section trailing edge, as is seen from the pressure curves.
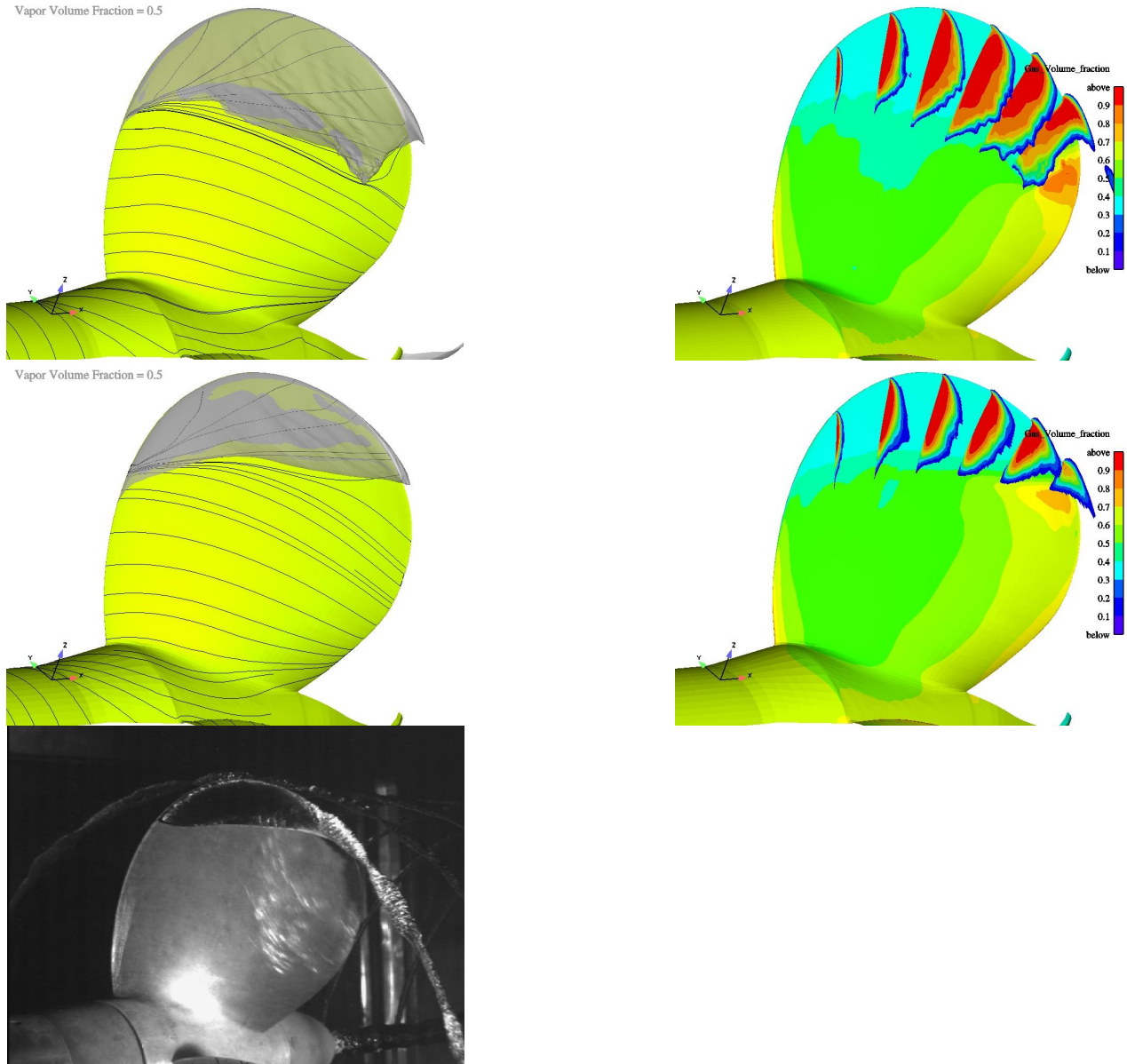
Figure 8: Cavitation behavior in uniform inflow at J = 0.71. In the left column: the transparent isosurface of vapor volume fraction α_v = 0.5 together with surface restricted streamlines. In the right column: axial cuts of the vaporized region colored by the vapor volume fraction. Top: first level fine grid results; middle: second level medium grid results; bottom: photograph of the cavitating propeller in the simulated conditions [1].

The cavitating regions are shown in Figure 8 by a transparent isosurface of vapor volume fraction $\alpha_v = 0.5$ for the two finest grid levels. Surface restricted streamlines are shown together with the vapor isosurface. Axial cuts of the vapor volume colored by the vapor volume fraction are also given in Figure 8. A photograph of the cavitating propeller in the simulated conditions is given for comparison.

The second level medium grid calculation gives a steady solution for the vaporized region. The first level fine grid solution is not steady; a small amount of vapor is shed at lower radii of the vaporized region near the trailing edge of the blade. The figures shown in this paper are taken at a moment when the cavity is at its average volume. In the cavitation tests the cavity was found to be stable.

It is seen that the predicted cavitating region is in reasonable accordance with the cavitation tests although the predicted vaporized region is somewhat larger in the simulations. The cavitating tip vortex is not captured in the calculations due to the coarse grid in the slipstream of the propeller. The surface restricted streamlines show that no re-entrant or side entrant jets are present in the cavity.

The axial cuts of the vaporized region reveal that the thickness of the vaporized region increases towards the trailing edge of the blade. It is also seen that the vaporized region is larger in the first level fine grid results.

Propeller in a wake field

The calculations for the propeller working in a wake field are performed in the wetted and cavitating conditions using a cavitation number $\sigma_n = 4.455$. The propeller rotational rate is 30.5 rps and the inflow velocity 6.22 m/s, which corresponds to the advance number $J = 0.90$. In these conditions cavitation occurs only when a blade is passing through the wake field.

LDV measurements of the total wake are performed by INSEAN. The total wake was measured between the wake generator and the propeller on an axial plane located at $x/R = -0.52$ upstream from the propeller plane.

Figure 9 shows the calculated and measured axial total wake distributions at the measurement plane non-dimensionalized by the free stream velocity. It is seen that the effect of the horizontal bars on the total wake is much higher in the calculations than in the measurements. The calculations are performed only on the second level medium grid at the time of delivering the paper. It is likely that the simulation for the first level fine grid would give a total wake closer to the measurements. Anyway, the width of the calculated total wake is relatively well captured in the medium grid calculations.
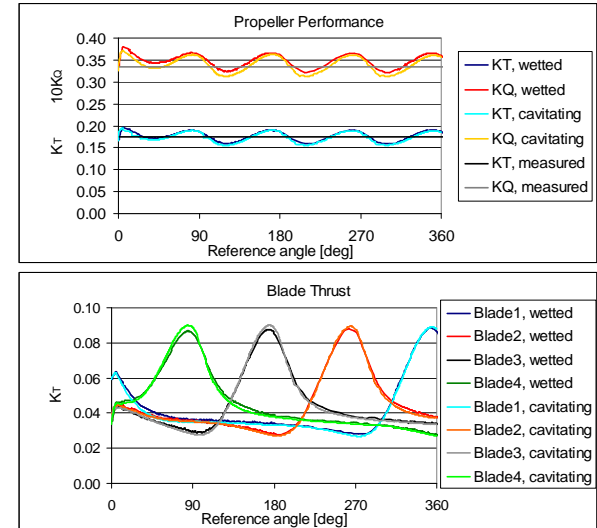
Figure 10 shows the propeller thrust and torque history in wetted and cavitating conditions over one propeller revolution when working in the wake field. The measured average thrust and torque in the wetted conditions are also given. Figure 10 also gives the thrust history for individual blades as a function of the propeller revolution angle. The initial states have been calculated using the quasi-steady approach. The calculations are continued for two propeller revolutions, but the histories are shown over only one revolution to give clearer performance figures.

It is seen from Figure 10 that loading has reached its final periodic shape after about a ¼ of one propeller revolution. The propeller loading period is 90° according to the four-bladed propeller. The propeller loading is at its highest when a blade is at the -10° position, i.e. 10° before reaching the 12 o'clock position. The individual blade loading is at its highest at the -5° position.
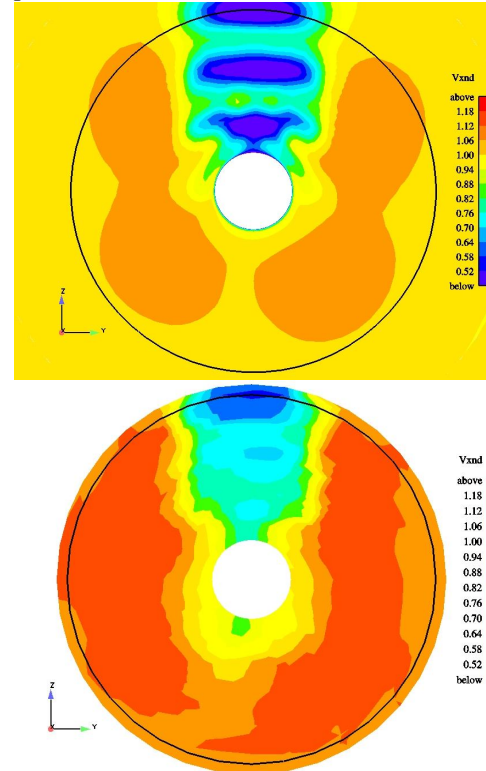
Figure 9: Calculated total axial wake (top) and measured total axial wake (bottom). The black circles refer to the propeller tip radius. The calculation result is for the second level medium grid.


Figure 10: Thrust and torque convergence history for the whole propeller (top) and for individual blades (bottom). The thrust and torque are given for the wetted and cavitating conditions. For the whole propeller the measured average thrust and torque are also shown in wetted conditions. The results are for the second level medium grid.
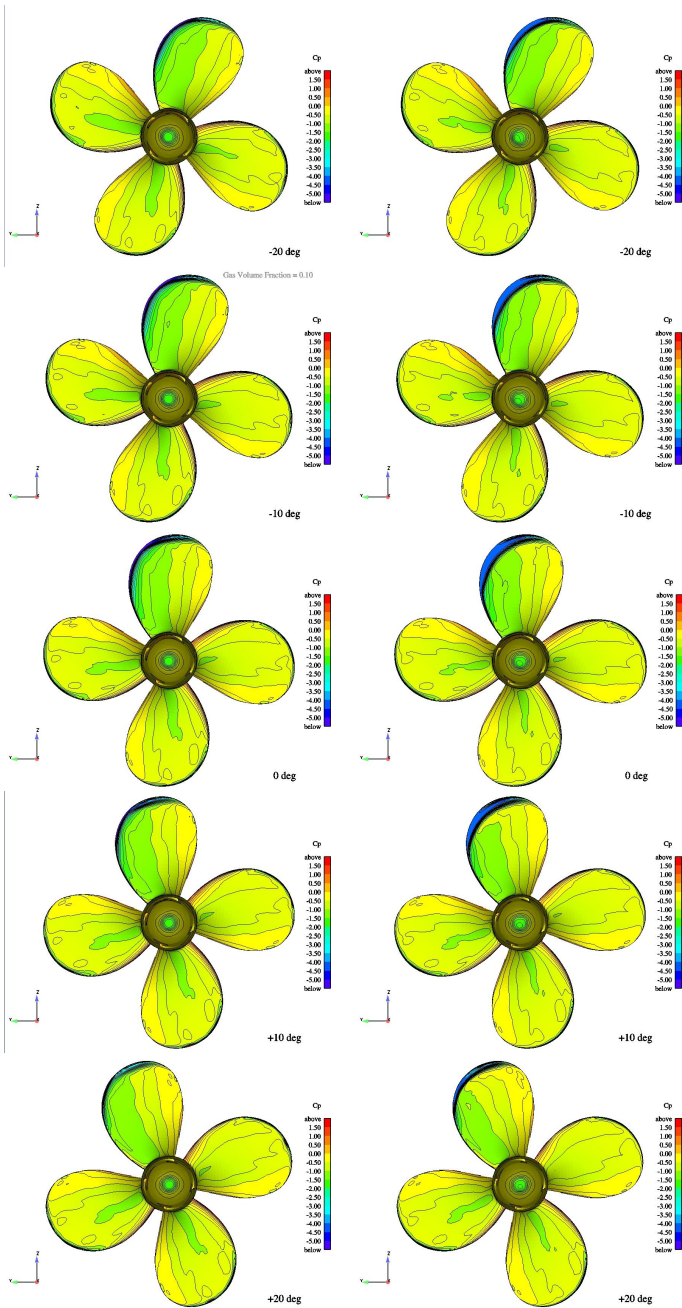
Figure 11: Propeller pressure distribution in the wake field. In the left column: wetted condition. In the right column: cavitating condition. From top to bottom: blade at -20°, -10°, 0°, +10° and +20° position, where 0° refers to a blade at the 12 o'clock position. The reference angle increases in the propeller rotational direction. The wake generator is at the 12 o'clock position but is not shown to give a clear view of the blades. The results are for the second level medium grid.

It is seen that cavitation has very little influence on the global performance of the propeller in the simulations. That is because the cavitation region on the blades is small in the investigated conditions. The global performance of the propeller has not been measured in cavitating conditions.
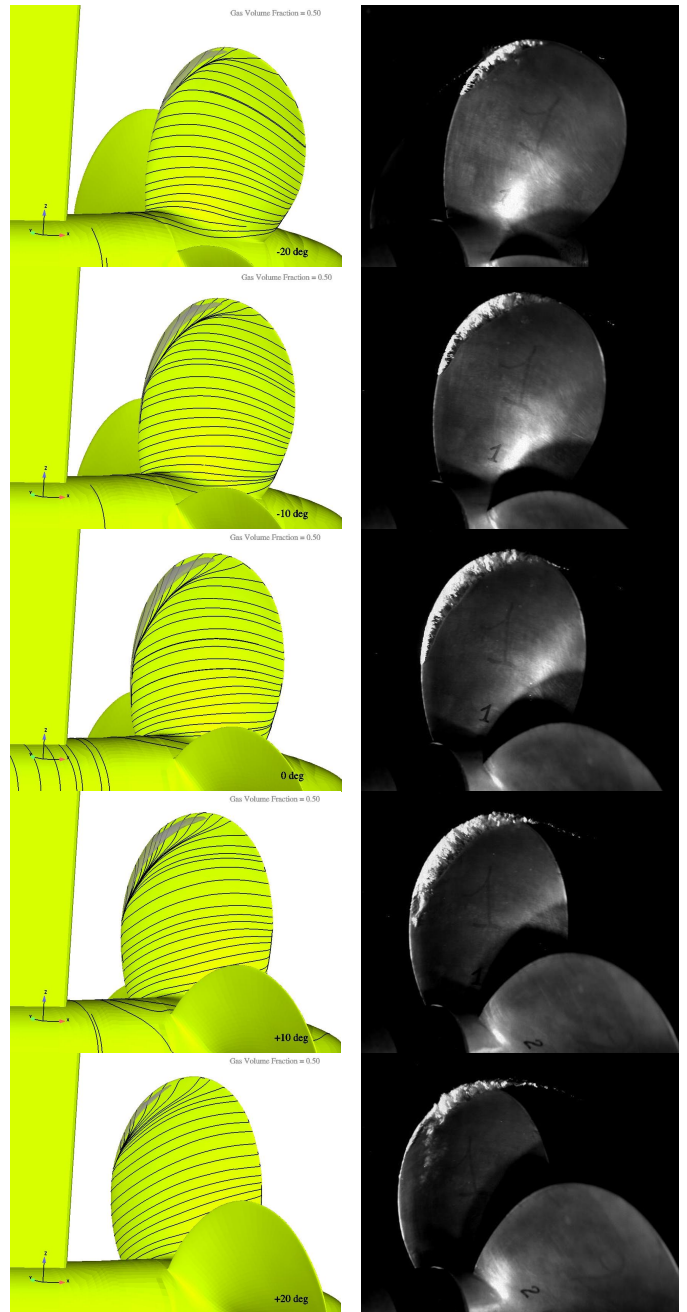
Figure 12: Propeller cavitation behavior in the wake field. In the left column: surface restricted streamlines and isosurface of vapor volume factor of $\alpha_v = 0.5$. In the right column: photograph of a cavitating propeller in the simulated conditions [2]. From top to bottom: blade at -20°, -10°, 0°, +10° and +20° position, where 0° refers to a blade at the 12 o'clock position. The reference angle increases in the propeller rotational direction. The results are for the second level medium grid.

The calculated average thrust in wetted conditions is 0.4 % lower than in the measurements. The calculated torque is 2.8 % higher than in the measurements. The excellent agreement between the global performances is coincidental. The average velocity through the wake measurement plane between the radii specified by the axis and the propeller tip is 6.6 % lower in the

8

calculations than in the measurements. This means that the propeller is working in higher loading conditions in the simulations than in the tests.

Figure 11 shows the pressure distribution on the propeller's suction side in wetted and cavitating conditions. The figures are given for blade positions from -20° to +20° at 10° intervals. At position -20° the blade's leading edge is entering the wake of the wake generator and at position +20° the blade is leaving the wake field. The pressure distribution on blades outside the wake is very similar in wetted and cavitating conditions, since cavitation occurs only when a blade is passing through the wake. The low-pressure region on the blade in the wake is larger in cavitating conditions than in wetted conditions, as was the case in uniform inflow too.

Figure 12 shows transparent isosurfaces of vapor volume factor of $\alpha_v = 0.5$ together with surface restricted streamlines. Figure 12 also shows photographs of the propeller in the simulated conditions at the same relative blade positions as the illustrations of the simulation.

Cavitation is well captured in the simulation when the blade is penetrating the wake at the -20° and -10° positions. With the blade in the upward position the trend is correct but the vaporized region is under-predicted compared with the photograph. At the +10° position the leading edge of the blade is still inside the wake and the vaporized region is again under-predicted but shows correct trends. In the final position the blade's leading edge has passed the edge of the wake. The attached cavity at the leading edge of the blade remains in the simulations only and the detached cavity rolling up into the tip vortex in completely missed.

Calculations performed at the finest grid level are expected to capture more cavitation details in the simulation as well as the right magnitude of the wake, which will further improve the cavitation predictions. The quality of the wake is found to be crucial to the cavitation predictions in the VIRTUE Rome 2008 workshop [7].

The surface restricted streamlines show that side entrant jets are present in the cavity region in the simulations. Water flows between the cavity and the blade and rolls up into the tip vortex. This phenomenon can be seen in the photographs as well. Similar trends of the side entrant jets are also found when this particular case is analyzed by LES [11].

DISCUSSION

The Insean E779A propeller was analyzed by a RANS solver (FINFLO) in uniform and non-uniform inflow. The simulations were performed in wetted and cavitating conditions. The cavitation model used in this work was Merkle's model. The results are compared with the measurements made by INSEAN. The predicted cavitation behavior was compared with photographs of the cavitating propeller.

The global performance of the propeller was found to be reasonable well predicted over a range of advance numbers in wetted conditions. The predicted thrust and torque were within 5% of the measured ones. The calculated efficiencies were nearly the same as the measured ones.

In the uniform inflow simulations a grid refinement study was made to find the grid convergence of the low-pressure peak at the leading edge of the propeller. At the finest grid level there were about 20 cells around the leading edge radius, which was found to give reasonable grid convergence to the pressure peak. It is crucial to estimate the pressure peak at the leading edge correctly from the cavitation inception point of view.

The cavitation region was found to be somewhat over-predicted in the calculations for uniform inflow. Anyway, the cavitation region is physically reasonable in the calculations. Tip vortex cavitation was not captured in the simulations even though it was clearly present in the cavitation tests. A very dense grid should be created in the tip vortex region to reduce dissipation of the tip vortex. This work is excluded from this paper.

Cavitation increased the propeller thrust and torque in the uniform inflow simulations by widening the low-pressure region on the suction side of the blade compared with the wetted flow simulation. In the tests cavitation had almost no effect on the propeller thrust and torque.

The propeller was also analyzed when working in a wake field in wetted and cavitating conditions. In the cavitation tests the wake field was created by locating a wake generator consisting of five flat plates parallel to the axial direction upstream of the propeller. The geometry of the wake generator was modeled in the computational domain to create the wake in the calculations. The calculations were performed using a time-accurate approach with the sliding surface method.

The grid near the propeller was the same as in the uniform inflow calculations. The calculations were made only at the second level medium grid both in wetted and cavitating conditions.

The predicted total wake was too strong in the calculations. It is likely that the predicted total wake would be closer to the measurements if the first level fine grid calculations were performed. The calculated average thrust and torque were within a few per cent of the measured ones. That is a coincidence since the average inflow to the propeller is lower in the calculations than in the measurements.

In contrast to the uniform inflow calculations, the cavitation region was under-predicted in non-uniform inflow simulations. Cavitation occurred only in a small region on a blade when passing through the wake field. Cavitation had a minor effect on the propeller's global forces and moments compared with the wetted condition calculations.

Predicted cavitation behavior showed correct trends except that the roll-up of the detached sheet cavitation into a tip vortex was not captured at all when the blade was leaving the wake. The side entrant jets between blade and the cavity were captured in the calculations. These jets are also visible in the cavitation test observations. First level fine grid calculations are to be performed to find out whether more details of the cavity can be captured by means of RANS.

Merkle's cavitation model was utilized using constants $C_{prod} = C_{dest} = 100$ for evaporation and condensation, respectively. Fine tuning these constants may improve the convergence. This work is excluded from this paper but must be done in the future.

The motivation to model the complex geometry of the wake generator in the calculation domain was to validate FINFLO for calculations where a propeller is working behind a

ship in cavitating conditions. It seems that FINFLO has capabilities to calculate this kind of problem, but more development and validation work is still needed.

CONCLUSION

The conclusions of this work can be set out briefly as follows:

The low-pressure peak at the leading edge of a blade is sensitive to grid resolution. A very high resolution grid must be set around the leading edge radius to solve the cavitation inception correctly.

The predicted thrust and torque were within 5% of the measured ones in the uniform inflow simulations in wetted conditions. The cavitation prediction in uniform inflow showed correct trends but was somewhat over-predicted.

The propeller working in a wake field was calculated only on the second level medium grid. The total wake was too strong but the width of the wake was relatively well captured. The trends of the cavity were correct but the cavitating region was under-predicted. The roll-up of the detached sheet cavity was not captured at all. The results would probably improve if the first level fine grid calculations were performed. That will be done in the future.

ACKNOWLEDGMENTS

NOMENCLATURE

Latin symbols

A	parameter in Antoine's equation
B	parameter in Antoine's equation
C	parameter in Antoine's equation, parameter in Merkle's cavitation model
C_P	pressure coefficient,

$$C_p = \frac{p - p_\infty}{\frac{1}{2}\rho_w (nD)^2}$$

D	propeller diameter
J	advance number, $J = \dfrac{V_{in}}{nD}$
k	kinetic energy of turbulence
K_Q	torque coefficient, $K_Q = \dfrac{Q}{\rho_w n^2 D^5}$
K_T	thrust coefficient, $K_T = \dfrac{T}{\rho_w n^2 D^4}$
L	length
n	propeller rate of revolutions (rps)
p	pressure
Q	torque
r	radial distance
R	propeller radius, radius
t	time
T	temperature, thrust
$\overset{\iota}{V}$	velocity
x	axial distance
y^+	non-dimensional wall distance

Greek symbols

α	phase volume factor
Γ	mass transfer term
ε	dissipation of turbulence
η_O	open water efficiency
ρ	density
σ_n	cavitation number, $\sigma_n = \dfrac{p_\infty - p_v}{\frac{1}{2}\rho_w (nD)^2}$
$\overset{\iota}{\tau}$	viscous stress tensor

subscripts

dest	destruction
l	liquid
in	inflow
m	mixture
prod	production
tun	tunnel
v	vapor
w	water
∞	infinity

REFERENCES

[1] Pereira, F., Salvatore, F., Di Felice, F., 2004, "Measurement and Modelling of Propeller Cavitation in Uniform Inflow," *Trans. ASME, J. of Fluids Engineering,* 126(4), 671-679.

[2] Pereira, F., Di Felice, F., 2004, "Experimental Investigation of a Cavitating Propeller in Non-Uniform Inflow," *26th Symposium on Naval Hydrodynamics,* St John's.

[3] Sanchez-Caja, A., Rautaheimo, P., Siikonen, T., 2000, "Computation of Incompressible Viscous Flow Around a Ducted Propeller Using a RANS Equation Solver," *23rd Symposium on Naval Hydrodynamics*, Val de Reuil, Vol. 3(2), pp.1-12.

[4] Siikonen, T., Hoffren, J., Laine, S., 1990, "A Multigrid LU Factorisation scheme for the thin-layer Navier-Stokes Equations," *Proc. 17th ICES Congress,* Stockholm, Vol.90-6.10.3, pp. 2023-2034.

[5] Merkle, C.L., Feng, J., Buelow, P.E.O., 1998, "Computational Modeling of the Dynamics of Sheet Cavitation," *Third International Symposium on Cavitation,* Grenoble.

[6] Streckwall H., Salvatore F., 2007 "Results of the Wageningen Workshop on Propeller Open Water Calculations Including Cavitation" *RINA Marine CFD*, Southampton, UK.

[7] Salvatore, F., Streckwall, H., Van Terwisga, T., 2009, "Propeller Cavitation Modelling by CFD – Results from the VIRTUE 2008 Rome Workshop", *First International Symposium on Marine Propulsors SMP'09*, Trondheim, Norway, (with INSEAN and HSVA).

[8] Chien, K.-Y., 1982, "Predictions of Channel and Boundary-Layer Flows with a Low Reynolds Number Turbulence Model," *AIAA Journal,* Vol. 20.

[9] Lindstrom, P.J., Mallard, W.G., 2005, *Eds., NIST Chemistry WebBook*, *NIST Standard Reference Database Number 69*, National Institute of Standards and Technology, Gaithersburg MD, http://webbook.nist.gov.

[10] Berchiche, N., Janson, C.-E., 2008, "Grid Influence on the Propeller Open-Water Performance and Flow Field," *Ship Technology Research,* Vol. 55, pp. 87 - 96.

[11] Bensow, R., Huuva, T., Bark, G., Liefvendahl, M., 2008, "Large Eddy Simulation of Cavitating Propeller Flows," *27th Symposium on Naval Hydrodynamics,* Seoul, Vol. 2 pp.151 - 168.